

Suzaku Observations of M82 X-1 : Detection of a Curved Hard X-ray Spectrum

Ryohei MIYAWAKI,¹ Kazuo MAKISHIMA,^{1,2,3} Shin'ya YAMADA,¹ Poshak GANDHI,²
Tsunefumi MIZUNO,⁴ Aya KUBOTA,⁵ Takeshi TSURU,⁶ and Hironori MATSUMOTO⁶

¹ *Department of Physics, The University of Tokyo, 7-3-1 Hongo, Bunkyo-ku, Tokyo 113-0033*

² *Cosmic Radiation Laboratory, Institute of Physical and Chemical Research (RIKEN),
2-1 Hirosawa, Wako-shi, Saitama 351-0198*

³ *Research Center for the Early Universe (RESCUE), The University of Tokyo,
7-3-1 Hongo, Bunkyo-ku, Tokyo 113-0033*

⁴ *Department of Physical Science, School of Science, Hiroshima University,
1-3-1 Kagamiyama, Higashi-Hiroshima, Hiroshima 739-8526*

⁵ *Department of Electronic Information Systems, Shibaura Institute of Technology,
307 Fukasaku, Minuma-ku, Saitama-shi, Saitama 337-8570*

⁶ *Department of Physics, Kyoto University, Kitashirakawa-Oiwake-cho,
Sakyo-ku, Kyoto 606-8502
mazima@phys.s.u-tokyo.ac.jp*

(Received 2008 July 0; accepted 2008 September 0)

Abstract

A report is presented on Suzaku observations of the ultra-luminous X-ray source X-1 in the starburst galaxy M82, made three times in 2005 October for an exposure of ~ 30 ks each. The XIS signals from a region of radius $3'$ around the nucleus defined a 2–10 keV flux of 2.1×10^{-11} erg s $^{-1}$ cm $^{-2}$ attributable to point sources. The 3.2–10 keV spectrum was slightly more convex than a power-law with a photon index of 1.7. In all observations, the HXD also detected signals from M82 up to ~ 20 keV, at a 12–20 keV flux of 4.4×10^{-12} erg s $^{-1}$ cm $^{-2}$. The HXD spectrum was steeper than that of the XIS. The XIS and HXD spectra can be jointly reproduced by a cutoff power-law model, or similar curved models. Of the detected wide-band signals, 1/3 to 2/3 are attributable to X-1, while the remainder to other discrete sources in M82. Regardless of the modeling of these contaminants, the spectrum attributable to X-1 is more curved than a power-law, with a bolometric luminosity of $(1.5 - 3) \times 10^{40}$ erg s $^{-1}$. These results are interpreted as Comptonized emission from a black hole of 100 – 200 solar masses, radiating roughly at the Eddington luminosity.

Key words: balck hole physics—galaxies:individual:M82—X-rays:stars

1. Introduction

Ultra-luminous compact X-ray sources (ULXs; e.g., Makishima et al. 2000), found in many nearby galaxies, are often considered as candidate intermediate-mass black holes (BHs), because their typical luminosity reaching 3×10^{39} to 10^{41} erg s $^{-1}$, calculated assuming isotropic radiation, largely exceeds the Eddington limit for known stellar-mass BHs. Since the first discovery by the Einstein satellite (Fabbiano 1989), ULXs have been studied extensively in soft X-rays with ROSAT (Colbert, Mushotzky 1999; Colbert, Ptak 2002; Liu, Bregman 2005; Liu et al. 2006), and then in energies up to ~ 10 keV with ASCA (Makishima et al. 2000; Mizuno et al. 2001), Chandra (e.g. Swartz et al. 2004), XMM-Newton (e.g. Feng, Kaaret 2005; Stobbart et al. 2006), and Suzaku (Mizuno et al. 2007; Isobe et al. 2008). Searches for their counterparts have also been carried out in the optical (e.g. Pakull, Mirioni 2003; Ptak et al. 2006) and radio (e.g. Sánchez-Sutil et al. 2006) wavelengths. In contrast, we have little information on ULXs in hard X-rays above 10 keV,

where the established mass-accreting BHs, including both stellar-mass ones and active galactic nuclei (AGNs), are known to emit a considerable fraction of their radiative luminosity.

Among a number of ULXs known so far, so-called source X-1 in the starburst galaxy M82 is the most extreme object, as the luminosity reached 10^{41} erg s $^{-1}$. Although the host galaxy M82 has been observed repeatedly with the past X-ray observatories due to its nearby location (~ 3.6 Mpc; Freedman et al. 2004) and its active star formation, the bright diffuse thermal X-rays from this galaxy hampered the detection of X-1 till the ASCA era. The presence of this object, X-1, was first suspected by Tsuru et al. (1997), based on differences of fluxes measured with EXSOAT, Ginga, and ASCA. Subsequently, the object was confirmed as a variable hard source through multiple ASCA observations, and interpreted at first as an active galactic nucleus veiled by the thermal plasma emission (Matsumoto, Tsuru 1999; Ptak, Griffiths 1999). However, thanks to the superb angular resolution of Chandra, it was later revealed to be a non-AGN source located ~ 170 pc

off the dynamical center of the galaxy (Matsumoto et al. 2001; Kaaret et al. 2001; Tsuru et al. 2004).

To explain the highest luminosity (1×10^{41} erg s $^{-1}$ in 3–20 keV; Rephaeli, Gruber 2002) recorded from M82 X-1, a mass of at least $700 M_{\odot}$ is necessary assuming isotropic radiation with a sub-Eddington luminosity. Moreover, the 54 mHz X-ray quasi-periodic oscillation (QPO), detected with XMM-Newton and RXTE (Strohmayer, Mushotzky 2003; Fiorito, Titarchuk 2004; Mucciarelli et al. 2006; Dewangan et al. 2006; Kaaret et al. 2006), suggests that the source, presumably a BH, has a mass of 100–300 M_{\odot} , assuming the QPO frequency to scale inversely with the BH mass. These results, together with a recent study of variability pattern (Casella et al. 2008), make M82 X-1 the most promising candidate for an intermediate-mass BH. It is also suggested to have a 62 day periodicity (Kaaret et al. 2006).

Spectral studies of M82 X-1 have been conducted extensively. With ASCA and XMM-Newton, however, such attempts were limited to relatively narrow bands, e.g., 2–10 keV, because of the surrounding bright thermal X-rays. As a result, the observed spectra were reproduced by a variety of spectral models, including a power-law (PL) of photon index $\Gamma = 1.7 - 2.5$ (Matsumoto, Tsuru 1999; Dewangan et al. 2006), a thermal plasma emission model with a temperature 4–11 keV (Matsumoto, Tsuru 1999), an unsaturated Comptonization model (Fiorito, Titarchuk 2004; Agrawal, Misra 2006), and slim-disk emission (Okajima et al. 2006). Since these modelings imply vastly different physical conditions of the emission region, the nature of M82 X-1 has remained ambiguous. For example, the slim-disk modeling by Okajima et al. (2006) leads to a BH mass of $\sim 30 M_{\odot}$, which is significantly lower than is implied by the other arguments. Another complication with X-1 is that it is heavily confused with other point sources in the core region of M82.

These confusion problems have been resolved by Chandra with its high angular resolution. In fact, Kaaret et al. (2006) found that the 0.3–8 keV band spectrum of X-1 can be represented by a PL model of a photon index $\Gamma \sim 1.7$. Nevertheless, the information is still insufficient to arrive at a clear scenario as to the nature of X-1.

Evidently, the detection of X-1 in harder energies is of crucial importance. The Large Area Counter onboard Ginga, sensitive over the 2–30 keV energy band, detected signals up to ~ 20 keV from the M82 galaxy, and yielded a spectrum which is better described by a thermal bremsstrahlung model of temperature ~ 5.7 keV than by a single PL model (Tsuru 1992). The emission, interpreted at that time as arising from a thin hot plasma, is now more likely to be attributable primarily to X-1. Cappi et al. (1999) successfully described a 3–30 keV BeppoSAX spectrum of M82 by a thermal plasma model of temperature ~ 8.2 keV. Furthermore, RXTE observations of M82 on 30 occasions yielded 3–50 keV spectra (Rephaeli, Gruber 2002); the spectra acquired in brighter and fainter phases were both reproduced by thermal plasma models, with a temperature of ~ 6.6 and ~ 7.4 keV, respectively. These existing results in harder energies commonly in-

dicating mildly curving broad-band spectra, rather than a PL-like one. However, the fields-of-view (FOVs) of these non-imaging instruments also contained the spiral galaxy M81, hosting a low-luminosity AGN (Ishisaki et al. 1996; Pellegrini et al. 2000; La Parola et al. 2004), located 37' away from M82. Therefore, possible contamination to the observed signal was not excluded.

The Hard X-ray Detector (HXD; Takahashi et al. 2007; Kokubun et al. 2007) onboard Suzaku (Mitsuda et al. 2007), with its unprecedented sensitivity in a broad (10–600 keV) energy band and a tightly collimated FOV of $34' \times 34'$ (FWHM), is expected to provide improved hard X-ray information on M82 X-1. Here, we report on the Suzaku detection of M82 X-1 up to ~ 20 keV, and interpret the results in terms of an intermediate-mass BH.

2. Suzaku Observations and Data Reduction

We observed M82 with Suzaku three times in the Science Working Group (SWG) phase; on 2005 October 4 UT11:50 through October 5 UT03:24, October 19 UT00:40–22:32, and October 27 UT11:05 through 28 UT02:24. Aiming primarily at the study of hot-gas outflows from M82, the three observations were all conducted with the XIS optical axis pointed at $(\alpha^{2000}, \delta^{2000}) = (9^{\text{h}}55^{\text{m}}34^{\text{s}}, 69^{\circ}45'53'')$, which is $\sim 5'$ north of the galaxy. The XIS results on this offset region have already been published as Tsuru et al. (2007). In the present paper, we focus on the central region of this galaxy, including in particular X-1.

Figure 1 shows an XIS 0 image in the 2–10 keV band from the second observation. The X-ray bright part coincides with the central region of M82, including luminous X-ray sources such as X-1. The M81 nucleus during this observation was right on the edge of the HXD-PIN FOV, where the transmission is $\leq 1\%$ even considering attitude uncertainties. Similarly, the HXD-PIN transmission for M81 was $\leq 3\%$ both in the first and third observations. As shown in the figure, two ULXs known in the present sky region, M81 X-6 and Holmberg XI X-1 (= M81 X-9; Fabbiano 1988a), were both outside the HXD-PIN FOV.

We used the software package HEADAS version 6.3.1 and xselect version 2.4 to extract light curves, images, and spectra, and xspec version 11 to analyze the spectra. The XIS and HXD datasets were screened by the revision 1.2 pipeline processing using the standard criteria as follows. Events were discarded if they were acquired under the South Atlantic Anomaly (SAA), or at regions of low cutoff rigidity (≤ 6 GV for XIS and ≤ 8 GeV c $^{-1}$ for HXD), or with the Earth elevation angle of $< 5^{\circ}$, or during those periods when the telemetry was saturated. The XIS events were further excluded when the source elevation above the sunlit Earth is $< 20^{\circ}$, and finally events with grade 0, 2, 3, 4, and 6 were selected. After these screenings, the three observations gave effective exposure of 29 ks, 36 ks, and 26 ks with the XIS, while 24 ks, 31 ks, and 22 ks with the HXD.

3. Data Analysis and Results

3.1. XIS Data Analysis

We extracted on-source XIS events from a region of $3'$ radius centered on the M82 nucleus, and background events from another region of $3'$ radius which is free from the diffuse X-ray emission associated with M82. In figure 1, these two regions are indicated by dashed circles. We utilize events from all four CCD cameras, after co-adding those from the three FI cameras (XIS 0, XIS 2, and XIS 3) which have virtually identical responses.

3.1.1. XIS light curves

Figure 2 shows 2–10 keV XIS 0 light curves obtained in the three observations. The background counts are negligible ($\leq 2\%$), compared to the signal counts which were determined as 0.460 ± 0.007 , 0.489 ± 0.006 , and 0.425 ± 0.007 cts s^{-1} in the three observations (the errors being 90% confidence ranges). Thus, the signal on the second and third occasions are higher by $\sim 6\%$ and lower by $\sim 8\%$, respectively, than that in the first observation. By fitting these light curves with a constant, we obtained $\chi^2/\text{d.o.f}$ (degree of freedom) of 95.7/95, 190.0/131, and 110.1/87, respectively. The probability of these signal counts being consistent with a constant value is $\sim 40\%$, 1%, and 5%, in the first, second, and third observations, respectively. Therefore, the source is likely to have varied during the second observation; in fact, the light curve suggests a gradual intensity increase by $\sim 10\%$ across the gross coverage of about one day.

3.1.2. XIS spectra

Figure 3 shows 0.5–10 keV spectra from the FI CCD (black; averaged over XIS 0, XIS 2, and XIS 3) and the BI CCD (gray; XIS 1), obtained by accumulating events over the source region of figure 1, and then subtracting those from the background region. To grasp the rough spectral properties, we tentatively summed up the three observations. Thus, the spectra are dominated by a rather hard continuum at energies above ~ 3 keV, whereas by line-rich softer thermal emission at lower energies. As confirmed through past observations, the hard continuum must be coming from luminous point X-ray sources including X-1 in particular, while the soft thermal emission from the diffuse hot plasmas (e.g., Tsuru et al. 1997; Moran et al. 1997; Griffiths et al. 2000; Stevens 2003; Ranalli et al. 2008; Strickland, Heckman 2007). A rough evaluation using a thermal model and a PL continuum indicates that the XIS spectra in energies above 3.2 keV (i.e., above $K\alpha$ line at 3.14 keV from H-like Ar) are contaminated by the thermal component by no more than 9%. Since we are interested in X-1, below we study the XIS spectra in the 3.2–10 keV range, discarding their softer part.

In the hard-band XIS spectra, we observe an emission line structure at 6–7 keV; this must be Fe-K lines, as reported in previous observations (e.g. Tsuru et al. 1997; Matsumoto, Tsuru 1999; Cappi et al. 1999; Rephaeli, Gruber 2002; Strohmayer, Mushotzky 2003; Agrawal, Misra 2006). Using the Chandra and XMM-Newton data, Strickland, Heckman (2007) spectrally resolved the iron line complex into 6.7 keV (from He-like iron) and 6.4 keV

(from nearly neutral iron) components, and showed that both are primarily distributed diffusely rather than associated with discrete sources.

3.2. HXD-PIN Data Analysis

Through the method described in section 2, we extracted the HXD-PIN data from the three observations. Although the data covers an energy range of 10–70 keV, we hereafter discard the lowest energy band of 10–12 keV, where the data are often affected by increased noise. Light curves and spectra are corrected for instrumental dead times after Takahashi et al. (2007) and Kokubun et al. (2007). In the present paper, we do not intend to analyze the HXD-GSO data, since the signals from M82 are estimated to be below the GSO detection limit. In addition, the HXD-GSO FOV becomes progressively wider above ~ 80 keV, and hence the contamination by M81 becomes difficult to eliminate.

3.2.1. Background subtraction

To perform background subtraction which is crucial for the HXD analysis, we utilized non X-ray background (NXB) models provided by the HXD detector team (Kokubun et al. 2007). When the present data analysis was carried out (Miyawaki 2008), there were two NXB models available, so-called *bgd_A* (Watanabe et al., suzakupemo-2007-01) and *bgd_D* (dead-time uncorrected; Fukazawa et al., suzakupemo-2007-02), which employ different algorithms. We produced fake background events using the two NXB models, both under the same observing conditions as the actual data, and both utilizing the same auxiliary information such as the measured upper-discriminator hit rates. By processing the fake events through the same screening criteria as for the actual on-source data, we derived two NXB event sets for each observation. Then, *bgd_A* and *bgd_D* respectively gave 12–70 keV count rates of 0.46 and 0.45 cts s^{-1} on October 4, 0.49 and 0.48 cts s^{-1} on October 19, and 0.52 and 0.50 cts s^{-1} on October 27. Thus, the two NXB models agree within 4%. Hereafter, we employ *bgd_A* for our spectral analysis, because it tends to systematically over-predict the NXB than the other model in this particular observation, and hence is expected to yield more conservative results for sources like M82 X-1 that are close to the HXD-PIN detection limit.

We examined the NXB modeling accuracy utilizing Earth-occulted data, assuming the Earth to be “dark” for HXD-PIN. These data were extracted using the same criteria as for the on-source data, except that the Earth elevation angle was required to be $< -5^\circ$ instead of $> 5^\circ$. The attained exposure was 5.3 ks on October 19 and 1.3 ks on October 27, while the October 4 data were free from Earth occultations. Figure 4 compares the observed Earth-occultation data, with the synthetic *bgd_A* spectra which emulate the NXB to be observed during these occultation periods. The observed and modeled NXB count rates in the 12–70 keV energy range are 0.56 ± 0.02 and 0.55 cts s^{-1} respectively on October 19, and 0.54 ± 0.04 and 0.54 cts s^{-1} on October 27 likewise, where the errors refer to 90% confidence levels. Statistical errors associated

with the NXB model are neglected, because the model produces 10 times larger number of fake events. When the energy band is limited to 12–20 keV, where signals are detected as described later, the observed and modeled NXB count rates become 0.31 ± 0.01 and 0.31 cts s^{-1} respectively on October 19, and 0.30 ± 0.03 and 0.30 cts s^{-1} on October 27 likewise.

As confirmed above, the Earth-occultation data and the modeled NXB data agree well with each other within statistic errors, which are 4% and 10%, on October 19 and 27, respectively. This statement applies both to the 12–70 keV and 12–20 keV bands. Further considering the NXB modeling accuracy of HXD-PIN which is generally $\sim \pm 5\%$ (Mizuno et al. 2007), and the 4% difference between the two NXB models, we hereafter regard that the NXB model correctly reproduces the HXD-PIN NXB within a systematic error of at most 4%.

3.2.2. HXD signal count rates

After the above preparations, we accumulated the on-source HXD-PIN data of M82, and derived 12–20 keV count rates from the three observations. In table 1, these results are compared with the NXB model predictions in the same energy band. In all three observations, the on-source data exhibit an excess count rate by ~ 0.04 cts s^{-1} above the modeled NXB. Of these excess counts, we expect 0.018 cts s^{-1} to be coming from the cosmic X-ray background (CXB), as calculated from the HEAO-1 results (Boldt 1987; Gruber et al. 1999). Further subtracting this CXB contribution, we are finally left with 0.016 – 0.027 cts s^{-1} (table 1) in 12–20 keV to be attributable to the net signals from M82. Although the 12–20 keV CXB intensity within the HXD-PIN FOV is expected to fluctuate by $\sim \pm 12\%$ (rms) from sky to sky, this is only to $\pm 1\%$ of the NXB in the same energy range, because the average CXB count rate therein, typically 7% of the NXB, is already low. Thus, the CXB fluctuation is negligible.

The PIN signals, remaining after subtracting the NXB and CXB, have statistical significance of 3 to 5 sigmas on individual observations, and 8 sigmas when the three data sets are summed together. Furthermore, the implied 12–20 keV signal rates, ~ 0.02 cts s^{-1} , amount to 6–10% of the NXB count rate in the same band. This exceeds the typical NXB reproducibility during the present observations, 4%, as estimated in section 3.2.1. Therefore, the positive signals are thought to be significant even considering the systematic NXB errors.

After we had completed our data analysis, the background model *bgd_D* was updated, by taking into account dead-time correction and improving the estimation method (Mizuno et al., *suzakumemo-2008-03*). Accordingly, we re-generated the background files using this improved method, to find that it gives essentially the same results as the previous *bgd_D*. Therefore, we retain our original choice of *bgd_A*, which tends to overestimate the NXB and hence gives more conservative results. We later examine the effects of these different background models by artificially changing the NXB by $\pm 4\%$.

3.2.3. HXD light curves

As described in section 3.1, the XIS signal from the central region of M82 exhibited rather small (if any) variations during the present observations. Supposing that the positive HXD-PIN signals, as revealed above, are also coming from an approximately identical region in M82, we expect rather constant count rates as well. If, on the other hand, the positive HXD-PIN counts were an artifact of wrong NXB subtraction, they would vary with time typically on time scales of minutes to hours, just reflecting those in the NXB (Kokubun et al. 2007). For this purpose, the 12–20 keV PIN light curves of the three observation were derived, and presented in figure 5 together with the behavior of the modeled NXB.

On all occasions, the background-subtracted counts in figure 5 thus show on-average positive values, which agree with those in table 1. Furthermore, the net signal (green) appears relatively constant within statistical errors, in contrast to significant raw-count variations (black) that reflect those in the NXB (red). When fitted with a constant, these background-subtracted light curves yield $\chi^2/\text{d.o.f}$ of 41.7/28, 42.8/39, and 31.2/30, in the first, second, and third observations, respectively. These imply probabilities of $\sim 5\%$, 35%, and 40% for the light curves to be consistent with being constant. Thus, we consider that the positive HXD-PIN counts listed in table 1 persisted throughout the observations, while the variable NXB was removed successfully.

In this way, we have carefully examined the HXD-PIN signals using the Earth-occultation data and the on-source light curves. The results confirm that the positive HXD-PIN signals above the CXB are real, and are coming from the M82 sky region.

3.2.4. HXD spectra

Figure 6 shows the full-range PIN spectra (black) from the three observations, compared with the corresponding NXB models (*bgd_A*; red). The figure also shows the NXB-subtracted data (green), and the predicted CXB spectrum (blue) based on the HEAO-1 results (Boldt 1987; Gruber et al. 1999). Thus, after the NXB subtraction, positive signals remain up to ~ 30 keV in all three observations. Furthermore, the signal exceeds the expected CXB at least up to ~ 20 keV. In the 12–20 keV band, these spectra imply an average signal count rate of ~ 0.023 cts s^{-1} above the CXB. This value agrees with that derived from the simple count-rate measurements (section 3.2.2; table 1), and the light curve analysis (section 3.2.3).

3.3. Spectral Model Fitting Analyses

In this subsection, we perform model fitting first to the XIS spectra, and then to those of HXD-PIN, both averaged over the 3 days. Afterwards, the XIS and HXD-PIN spectra are jointly analyzed.

3.3.1. Model fits to the XIS spectra

Among the three observations, the 3.2–10 keV XIS spectra differ to some extent in their normalization; as inferred from figure 2, those of the 2nd and 3rd observations are higher by 2.1% and lower by 10.6%, respectively, than that of the first occasion. However, after scaling by these

factors, the three spectra agree with one another within their errors, which are typically 5% per channel under the present binning. Therefore, we hereafter analyze the XIS spectra summed over the 3 observations.

We jointly fitted the 3.2–10 keV XIS FI and BI spectra, thus summed over the three observations, with a model consisting of a PL for the continuum and two Gaussians for the Fe- K_α lines. The XIS response file and the associated ancillary file was generated with “xismrfgen” and “xissimarfgen” tool, respectively (Ishisaki et al. 2007). We constrained the overall model normalization to be the same between the FI and BI detectors. The hydrogen column density describing photoelectric absorption is here and hereafter fixed at $1.1 \times 10^{22} \text{ cm}^{-2}$, as determined with Chandra (Kaaret et al. 2006) under the least contamination by the diffuse emission: this amount of absorption attenuates the continuum at 3.2 keV only by 10%, and if treated as a free parameter, the absorption would couple too strongly with the continuum slope. The model yielded a fit as shown in figure 7 (left), with the best-fit parameters summarized in table 2 under the column of “XIS-only”. Thus, the PL photon index became $\Gamma = 1.67$. Although not given in the table, one Gaussian is centered at an energy of 6.67 ± 0.02 keV, with an intrinsic width (in Gaussian sigma) of < 0.11 keV and an equivalent width (EW) of 59 ± 11 eV. Its inclusion improved the fit by $\Delta\chi^2 \sim 88$. The other Gaussian, with its energy fixed at 6.4 keV and assumed to be narrow, exhibited an EW of 19 ± 8 eV, and improved the fit by $\Delta\chi^2 \sim 15$.

The 2–10 keV flux detected with the XIS, averaged over the three data sets, becomes $2.1 \times 10^{-11} \text{ erg s}^{-1} \text{ cm}^{-2}$, which yields a 2–10 keV luminosity of $3.4 \times 10^{40} \text{ erg s}^{-1}$ at 3.6 Mpc. This is typical of, or relatively lower than, those measured previously from narrow regions (depending on the angular resolution) around X-1, which scatter over $(1-6) \times 10^{-11} \text{ erg s}^{-1} \text{ cm}^{-2}$ (e.g. Griffiths et al. 1979; Watson et al. 1984; Fabbiano 1988b; Shcaaf et al. 1989; Tsuru 1992; Tsuru et al. 1997; Matsumoto, Tsuru 1999; Ptak, Griffiths 1999; Cappi et al. 1999; Matsumoto et al. 2001; Kaaret et al. 2001; Rephaeli, Gruber 2002; Strohmayer, Mushotzky 2003; Kaaret et al. 2006; Dewangan et al. 2006).

Although the above model approximately reproduces the observed XIS spectra, the fit is formally unacceptable with $\chi^2/\nu = 1.83$ (table 2). As shown in figure 7a, the model overpredicts the data above ~ 7 keV, suggesting the spectrum to have a more convex shape than a simple PL. Actually, the best-fit photon index becomes discrepant as 1.56 ± 0.03 and 2.0 ± 0.2 , when the fit energy range is restricted to 3.2–6.0 keV and 7–10 keV, respectively. The PL fit could be made acceptable by allowing the low-energy absorption to vary freely, but then the column density must become $\gtrsim 3.7 \times 10^{22} \text{ cm}^{-2}$, much exceeding the Chandra value of $1.1 \times 10^{22} \text{ cm}^{-2}$ (Kaaret et al. 2006). Therefore, the intrinsic continuum is suggested to be curved. To express such a convex shape, we fixed again the absorption to $1.1 \times 10^{22} \text{ cm}^{-2}$, and replaced the PL continuum by a cutoff PL model, namely a PL multiplied by an exponential cutoff factor. Then, as shown in

figure 7b and described in table 2, the fit has become acceptable with $\chi^2/\nu = 1.06$, yielding $\Gamma \sim 0.76$ and a cutoff energy of $E_{\text{cut}} = 5.8$ keV. Therefore, we conclude that the spectrum has a more convex shape than a PL.

3.3.2. Model fits to the HXD-PIN spectra

We conducted similar model-fitting analyses to the background (NXB+CXB) subtracted 12–20 keV PIN spectra, again summed over the three observations. The fit utilized a response matrix at the HXD nominal position, ae_hxd_pinhxnom_20060814.rsp, and an ancillary response file generated by the hxdarfgen tool. The latter takes into account the fact that the HXD FOV center is $\sim 5'.7$ offset from the M82 nucleus. Then, a PL model gave a successful fit with $\chi^2/\nu = 9.2/6$, yielding a photon index of $\Gamma = 3.4_{-0.8}^{+1.0}$ (statistical 90% confidence errors), and a 12–20 keV flux of $4.4 \times 10^{-12} \text{ erg s}^{-1} \text{ cm}^{-2}$. These become $\Gamma = 3.7_{-1.2}^{+3.1}$ and $1.9 \times 10^{-12} \text{ erg s}^{-1} \text{ cm}^{-2}$ if the NXB is artificially increased (over-subtracted) by 4%, while $\Gamma = 3.1_{-0.6}^{+0.6}$ and $6.7 \times 10^{-12} \text{ erg s}^{-1} \text{ cm}^{-2}$ when it is reduced (under-subtracted) by 4%. In any case, the implied spectral slope ($\Gamma = 3-4$) is significantly steeper than that found in the XIS range ($\Gamma = 1.67$), reinforcing the gradual spectral steepening found in the XIS band.

3.3.3. Joint fits to the XIS and PIN spectra

In order to best utilize the wide-band capability of Suzaku, we fitted the XIS and HXD spectra simultaneously, using respective averages over the three observations. Since the energy range becomes much expanded, we tried a larger variety of continuum models than employed so far. In all modelings, the two Gaussians were included in the same manner as in section 3.3.1. The model normalization was constrained to be the same between the XIS and HXD-PIN, because the HXD-PIN ancillary response file (section 3.3.2) has already taken into account the different FOVs between the two instruments (assuming that the HXD-PIN signal is coming from the M82 central region). The obtained fits are shown in figure 8, while the fit parameters are summarized in table 2 under the column of “XIS+PIN”. (The table also gives the results obtained without using the HXD data.) Furthermore, like in section 3.3.2, we considered the case where the NXB of HXD-PIN is systematically changed by $\pm 4\%$.

First, we tried a PL model, but the joint fit was not acceptable with $\chi^2/\nu \geq 2.6$ even allowing for the 4% NXB uncertainty (table 2). As shown in figure 8a, the model over-predicts the XIS and HXD-PIN data in the energy ranges of ≥ 7 keV. Although the fit is improved to $\chi^2/\nu \sim 1.9$ by tentatively allowing the model normalization to take separate values between the two instruments, the HXD vs. XIS normalization ratio then became ≤ 0.7 . This is too small, considering the XIS vs. HXD calibration uncertainties which are at most $\sim 15\%$ (Kokubun et al. 2007). Thus, the joint fit reinforces the inference made so far, that the X-1 spectrum is more convex than a PL. Below, we return to our original procedure of equalizing the model normalization between the two instruments.

Next, we tried an empirical thermal bremsstrahlung (bremss) model. Although the fit is better ($\chi^2/\nu = 1.3-2.2$ depending on the NXB systematic errors) than

the PL fit, the model is still over-predicting in the ≥ 7 keV energy range as shown in figure 8b. The obtained temperature, $T \sim 14$ keV, is higher than the values of 5–8 keV measured with Ginga (Tsuru 1992), BeppoSAX (Cappi et al. 1999), and RXTE (Rephaeli, Gruber 2002). These results remain essentially unchanged even when changing the PIN NXB by $\pm 4\%$.

Third, we employed a cutoff PL model. As shown in figure 8c and table 2, it has given $\chi^2/\nu = 1.07 - 1.26$, together with $\Gamma = 0.5 - 0.9$ and $E_{\text{cut}} = 4 - 8$ keV. Therefore, this model remains successful even including the HXD-PIN data. Because a cutoff PL gives an approximation to an unsaturated thermal Comptonization process of some soft seed photons, we replaced it with a thermal Comptonization model, called ‘‘CompTT’’ (Titarchuk 1994) in `xspec`. Since the input soft-photon energy is not well constrained by the present data, we fixed it to several values between 0.1 and 0.3 keV. Then, as presented in figure 8d, the fit was similarly acceptable with $\chi^2/\nu = 1.09 - 1.32$, and gave an electron temperature of $T_e = 2.3 - 2.9$ keV and an optical depth of $\tau = 7 - 9$; the results were essentially independent of the soft-photon temperature in the above-mentioned range. The obtained values of T_e and τ are both consistent with the XMM-Newton results on M82 X-1 by Agrawal, Misra (2006).

Finally, to evaluate a scenario of emission from an optically-thick accretion disk, we tested a ‘‘disk blackbody’’ (`diskbb`) model which represents multi-color blackbody emission from a standard accretion disk (Mitsuda et al. 1984; Makishima et al. 1986). As shown in figure 8e, the fit was rather poor with $\chi^2/\nu = 1.32 - 1.72$, because the model has too convex a shape and hence under-predicts the data in the higher energy range. To improve the fit, we then generalized the `diskbb` model to ‘‘variable- p ’’ model (Mineshige et al. 1994; Hirano et al. 1995; Kubota, Makishima 2004; Kubota et al. 2005; Okajima et al. 2006; Mizuno et al. 2007). It assumes that the disk temperature scales as r^{-p} , where r is the radius and p is a free parameter, with $p = 0.75$ corresponding to `diskbb`. It gives a good approximation to emission from a slim disk (Watarai et al. 2000; Ebisawa et al. 2003), which is expected to form under very high accretion rates. The fit has then become acceptable with $\chi^2/\nu = 1.09 - 1.24$ (figure 8f), and the obtained parameters, namely the inner-disk temperature $T_{\text{in}} = 3.4 - 3.6$ keV and $p = 0.61 - 0.65$, are consistent with those of Okajima et al. (2006) who applied the the same model to the XMM-Newton data of X-1 acquired at a similar luminosity to the present case.

From these studies, we have found three models that successfully and simultaneously reproduce the XIS and HXD-PIN data. A cutoff PL model with $E_{\text{cut}} \sim 5$ keV, a CompTT model invoking a relatively cool and thick electron cloud, and a variable- p model with a very high disk temperature. In all these cases, the two Gaussians were found to take nearly the same parameters as found with the XIS (section 3.3.1).

As seen from table 2, the addition of the HXD-PIN data have little affected the best-fit parameters of these successful models, with similar or somewhat reduced er-

rors. In contrast, their inclusion has allowed us to much more securely exclude the other unsuccessful models. In this sense, the XIS and HXD-PIN data are fully consistent with each other. When the NXB level is artificially changed by $\pm 4\%$, the fit goodness of all the three successful models degrades considerably. This reinforces the correctness of the NXB subtraction, unless the detected signal has a very complex broad-band continuum shape which requires a composite modeling.

3.4. Estimation of Contamination from Other Sources

Although we have so far quantified the broad-band Suzaku spectra, the results may not be totally ascribed to X-1, because the HXD-PIN data are likely to be contaminated by M81, as well as by other discrete sources in M82. The latter must contaminate the XIS data as well, because many of them are clustered in too narrow a region, $\sim 30''$ in radius around the M82 center, to be resolved with the XIS.

3.4.1. M81

As described in section 2 and illustrated in figure 1, the M81 nucleus was on the edge of the HXD-PIN FOV, with transmission of at most 1–3%. Therefore, the contamination is expected to be small, but may not be totally neglected.

Using BeppoSAX, Pellegrini et al. (2000) measured the 10–100 keV flux of the M81 nucleus as 7.4×10^{-11} erg s^{-1} cm^{-2} , and described its spectrum by a PL with $\Gamma \sim 1.84$. The 12–20 keV flux is implied to be 1.5×10^{-11} erg s^{-1} cm^{-2} . According to La Parola et al. (2004), furthermore, the M81 nucleus varied in the 0.5–2.4 keV band by a factor of 4 through past observations, and became up to ~ 1.4 times as bright as observed by Pellegrini et al. (2000).

Adopting an extreme assumption that the M81 nucleus was at its brightest level during the present observations, and that the spectrum retained $\Gamma \sim 1.8$, the angular transmission described in section 2 predicts this low-luminosity AGN to contribute up to $\leq (2 - 6) \times 10^{-13}$ erg s^{-1} cm^{-2} to the 12–20 keV HXD-PIN data. These correspond to 5–15% of the background-subtracted PIN flux (section 3.3.2). Taking an exposure-weighted mean over the three occasions, the M81 contamination to the HXD-PIN signal is estimated to be at most 10%. Since the PIN spectra in figure 8 have statistical errors of several tens percent per bin, and since M81 may not have been in the brightest phase, we conclude that the effect of the M81 nucleus is negligible. This is an advantage of the HXD with its tightly collimated FOV.

3.4.2. Other discrete X-ray sources in M82

Besides X-1, the central region within $\sim 30''$ of the M82 nucleus harbors about a dozen X-ray point sources more luminous than $\sim 10^{38}$ erg s^{-1} (Griffiths et al. 2000; Matsumoto et al. 2001; Kaaret et al. 2006; Strickland, Heckman 2007). To study their fluxes and spectra, and estimate their contamination to the present Suzaku results, we re-visited the Chandra archival data. By 2007 August, the central regions of M82 were observed six times with the Chandra ACIS for exposures longer than 10 ks; these are ObsID 361, 1302, 2933, 6097, 5644, and 6361. Using

the CIAO 3.4 software package and standard screening criteria, we extracted point sources which are located within $2'.9$ of X-1; these can contaminate both the present XIS and HXD spectra. Referring to the ROSAT PSPC image, any X-ray sources that are outside the XIS integration radius but within the HXD-PIN FOV are considered negligible.

Through this analysis, we confirmed the report by Kaaret et al. (2006) that a second brightest source, which they call X42.3+59, is located at $\sim 5''$ off X-1; we hereafter call it X-2. Across the six Chandra observations, the 2–10 keV flux of X-2 varied largely, from less than $\sim 10^{-13}$ erg s $^{-1}$ cm $^{-2}$ to 6.9×10^{-12} erg s $^{-1}$ cm $^{-2}$, with the latter amounting to 1/3 of the 2–10 keV XIS signal flux. As already reported by Kaaret et al. (2006), the 3–8 keV spectrum of X-2 at its brightest phase was described by a PL with $\Gamma \sim 1.3$, absorbed by a column of $N_{\text{H}} = (2 - 3) \times 10^{22}$ cm $^{-2}$, and a soft-excess component was required if lower energies are included.

Fainter X-ray sources, other than X-1 and X-2, were found to have a 2–10 keV luminosity of $\lesssim 3 \times 10^{39}$ erg s $^{-1}$ each. Among the six Chandra observations, their summed 2–10 keV flux remained relatively constant at $(7 - 9) \times 10^{-12}$ erg s $^{-1}$ cm $^{-2}$, which accounts for about 1/3 of the XIS signal. Their summed 3–8 keV spectrum was reproduced by a PL with $\Gamma = 1.5 - 1.7$.

As shown so far, we expect the fainter discrete sources to account for about 1/3 of the detected XIS signal. Furthermore, another 1/3 could be ascribed to X-2 if it is in the brightest phase. Therefore, the soft X-ray flux actually attributable to X-1 is estimated to be 2/3 (if X-2 is very faint) to 1/3 (if X-2 is brightest) of the detected 2–10 keV XIS signal of 2.1×10^{-11} erg s $^{-1}$ cm $^{-2}$ (section 3.3.1). These contaminants are expected to introduce a larger uncertainty to the HXD-PIN results, because their hard X-ray spectra cannot be measured separately. Below, we consider this issue assuming two extreme cases.

3.4.3. Re-evaluation of the spectra considering contamination

We first consider an extreme case where X-2 is faint enough to be neglected, and hence we need to consider only the fainter sources. If their summed spectrum determined with Chandra (a PL with $\Gamma = 1.5 - 1.7$) were extending into the hard X-ray range, the implied counts at 30 keV would reach $\sim 10\%$ of the HXD-PIN background, which is well above the systematic background uncertainty. Furthermore, the 30–40 keV signals, attainable with HXD-PIN in the 77 ks exposure (the three observations summed), would have a statistical significance exceeding 6 sigmas. Thus, we must have detected their signals at least up to ~ 40 keV, as illustrated in figure 9a. However, the actual 12–20 keV PIN spectrum was rather soft with $\Gamma \sim 2.5$, and was undetectable above ~ 20 keV. Therefore, the summed spectrum from the fainter sources should bend in energies above ~ 7 keV. This is reasonable, because these sources are considered to be mainly luminous low-mass X-ray binaries, of which the 2–20 keV spectrum is empirically approximated by a thermal bremsstrahlung model with a temperature of $T = 7 - 13$

keV (Makishima et al. 1989). Such a bremsstrahlung model has a mildly curved shape, and its 3–8 keV portion can be approximated by a PL with $\Gamma \sim 1.5$ (Makishima et al. 1989), in agreement with the Chandra measurement.

With the above consideration, we modeled the summed contribution of the faint sources by a $T = 10$ keV thermal bremsstrahlung model, of which the 2–10 keV flux was fixed at 8×10^{-12} erg s $^{-1}$ cm $^{-2}$ as specified by the Chandra data. Including this model as a fixed component, we jointly re-fitted the same Suzaku XIS and PIN spectra using the same family of models as in section 3.3.3. As shown in table 3 under the column “Case 1”, and presented in figure 9b, the obtained results are close to those obtained before. However, the inferred X-1 spectrum became softer, because the $T = 10$ keV thermal bremsstrahlung model, which is now subtracted away, is somewhat harder than the original wide-band Suzaku spectrum. As a result, not only the successful three models, but also the simple multi-color disk model with $T_{\text{in}} \sim 3.1$ keV, have become acceptable. Equivalently, the variable- p model gave $p \sim 0.75$, which just implies a standard accretion disk. After subtracting the contamination, the 2–10 keV flux attributable to X-1 becomes 1.2×10^{-11} erg s $^{-1}$ cm $^{-2}$, and the luminosity therein is 1.9×10^{40} erg s $^{-1}$.

As the other extreme, we may consider the case where the present observations happened to catch X-2 at its brightest level ever recorded by Chandra, and hence its contribution to the Suzaku spectra must be considered as well. Although the X-2 spectrum obtained by Chandra at the brightest epoch was rather hard ($\Gamma \sim 1.3$), it cannot keep extending into the > 10 keV energy range, for the same reason as discussed just above for the fainter sources. Thus, the X-2 spectrum is inferred to have a power-law shape in the 3–8 keV range, together with a high-energy turn over, and a soft excess (Kaaret et al. 2006). Such a spectral composition is typical of “PL state” ULXs (e.g., Feng, Kaaret 2005; Stobbart et al. 2006). Although these objects generally have a steeper range of spectra with $\Gamma = 1.6 - 2.5$, a case with $\Gamma \sim 1.4$ is known (Kubota et al. 2001b). Regarding X-2 as such an object, we decided to express its spectrum by a cutoff PL model with $\Gamma = 0.5$ and a cutoff energy of $E_{\text{cut}} = 5.0$ keV, absorbed with $N_{\text{H}} = 2.5 \times 10^{22}$ cm $^{-2}$ (Kaaret et al. 2006). The adopted cutoff energy is a typical value found among power-law type ULXs (Miyawaki 2008; Mizuno et al. 2007), and the photon index of 0.5 was chosen so that the model, of the form $\propto \exp(-E/E_{\text{cut}})E^{-\Gamma}$, mimics the $\Gamma = 1.3$ PL in the 3–8 keV band. Its normalization was adjusted to reproduce the Chandra flux.

Including these two fixed models (one for X-2 and the other for the fainter sources), we repeated the fitting procedure; the obtained results are presented in figure 9c, and the parameters are given in table 3 under the column denoted “Case 2”. Although the 2–10 keV flux attributable to X-1 further decreased to 7.0×10^{-12} erg s $^{-1}$ cm $^{-2}$, and its 2–10 keV luminosity to 1.1×10^{40} erg s $^{-1}$, the spectral results have remained mostly the same as the case of X-2 being negligible. This is because the assumed X-2 spec-

trum is relatively similar in shape to the original Suzaku XIS plus HXD-PIN spectra, as is clear from the cutoff PL fit parameters in table 2.

These studies confirm that the removal of the estimated contributions from X-2 (under the most extreme assumption) and the other fainter sources leaves significant 3–20 keV counts that are attributable to X-1. These remaining hard X-ray photons still form a clearly curved spectrum, which excludes a PL and a thermal bremsstrahlung modeling, similar to the case of ignoring the contamination. Thus, except for the normalization, our basic results on X-1 are relatively unaffected by the contaminating sources, in spite of apparently large uncertainties that they introduce. This is because we would encounter an unphysical condition of negative X-1 flux at ~ 20 keV if the contaminants had significantly harder spectra, while we can simply utilize the parameters in table 2 if the spectra of the contaminants were much softer and hence negligible in the HXD-PIN range.

4. Discussion

4.1. Summary of the results

With the Suzaku XIS, we detected a 2–10 keV flux of 2.1×10^{-11} erg s $^{-1}$ cm $^{-2}$ that is attributable to the assembly of luminous point sources within 3' of the nucleus of M82. Of this flux, about 2/3 can be accounted for by the sum of the two most luminous sources, X-1 and X-2, whereas the remaining 1/3 is ascribed to the other fainter ones. The share of 2/3 is totally attributable to X-1 if the highly variable X-2 was negligibly dim at that time, whereas it is further subdivided roughly equally between X-1 and X-2 if X-2 was at the brightest state ever recorded. We hence estimate the 2–10 keV flux of X-1 as $(7 - 14) \times 10^{-12}$ erg s $^{-1}$ cm $^{-2}$, and its 2–10 luminosity as $(1.1 - 2.1) \times 10^{40}$ erg s $^{-1}$ at 3.6 Mpc, both with a typical systematic uncertainty by a factor of two. The estimated luminosity of X-1 is similar to, or somewhat lower than, those so far measured from this source.

From a wider sky region including M82, we also detected significant hard X-ray emission with the Suzaku HXD-PIN, at a 12–20 keV flux of 4.4×10^{-12} erg s $^{-1}$ cm $^{-2}$. When summed over the three observations, the HXD-PIN signal (after subtracting the NXB and CXB) has a statistical significance of 8 sigmas, and about twice as high as the systematic background uncertainty. Therefore, the signal is considered real. The HXD data define a rather steep spectrum with $\Gamma = 3 - 4$.

The acquired HXD-PIN data are fully consistent with them coming from the same sources as detected with the XIS. Regardless of the way of removing the estimated contamination from X-2 and the fainter sources (section 3.4), the overall Suzaku spectrum, spanning 3–20 keV (with a narrow gap over 10–12 keV), is clearly more convex than a single PL, even though it can be approximated by a PL over a limited 3–8 keV range. This reconfirms previous broad-band studies with Ginga (Tsuru 1992), BeppoSAX (Cappi et al. 1999), and RXTE (Rephaeli, Gruber 2002), which all reported “thermal” type spectral shapes rather

than straight PL like ones. Clearly, relativistic jet emission, invoked by some authors (e.g., Krauss et al. 2005) to explain the behavior of some ULXs, is inappropriate at least in the case of M82 X-1, since the observed spectral curvature ($|\Delta\Gamma| \gtrsim 1$ across ~ 10 keV) is too strong to be attributable to synchrotron cooling or burn-off effects.

The curved spectrum of M82 X-1 can be expressed by either of the three successful continuum models; an empirical cutoff PL model, a thermal Comptonization model invoking a cool and thick electron cloud, and an optically-thick emission from a rather hot accretion disk (section 3.4). Details of their model parameters depend to some extent on the assumed broad-band spectra of the contaminants. Superposed on the continuum, we also detected two iron emission lines.

4.2. An interpretation of the curved spectrum

Although ULXs show a variety of spectral shapes, two prototypical spectral states have been recognized through past observations (e.g., Makishima et al. 2000; Sugihō 2003; Feng, Kaaret 2005; Dewangan et al. 2006; Stobart et al. 2006; Mizuno et al. 2007; Makishima 2007a; Makishima 2007b; Miyawaki 2008). One is “PL state”, wherein the spectrum below ~ 10 keV is approximated by a single PL model, but is often accompanied by a soft excess (e.g., Miller et al. 2003; Soria et al. 2007) as well as a mild turn-over toward higher energies (e.g., > 6 keV; Mizuno et al. 2007). We already argued in section 3.4.3 that the second brightest source, M82 X-2, is likely to be an object in the PL state. The other is “convex-spectrum (hereafter CS) state” (Makishima 2007a), in which the spectrum exhibits a significantly curved shape even in the limited energy range of ~ 1 to ~ 10 keV, so that an MCD model gives a better fit than a PL. The two ULX states are not considered to represent distinct classes of objects, since an increasing number of sources are confirmed to make transitions between these two spectral states (e.g., Makishima et al. 2000; Kubota et al. 2001b; Sugihō 2003; La Parola et al. 2004; Miyawaki 2008).

Mizuno et al. (2007) and Makishima (2007a) utilized Suzaku data on NGC 1313, to study spectral properties of two ULXs therein, X-1 and X-2. Then, X-2 was found in the CS state, and its 0.5–10 keV spectrum was represented successfully by a variable- p model with $p = 0.63 \pm 0.03$ and $T_{\text{in}} = 1.86 \pm 0.15$ keV. In contrast, the other source, X-1, was in the PL state, because its spectrum was much less convex (approximated by a PL with $\Gamma \sim 2.1$), with a hint of soft excess and a mild high-energy turn over. Thus, the XIS spectrum of NGC 1313 X-1 was reproduced successfully by a cutoff PL continuum with $E_{\text{cut}} = 3.41^{+0.57}_{-0.40}$ keV and $\Gamma = 0.89 \pm 0.20$, plus a cool ($T_{\text{in}} \sim 0.2$ keV) `diskbb` for the soft excess. The source exhibited a rather high 0.4–10 keV luminosity of 3.3×10^{40} erg s $^{-1}$.

As clarified in the present study, the Suzaku spectrum of M82 X-1 is approximated by a PL model with $\Gamma \sim 1.7$ in the limited 3–8 keV range, while it is reproduced by a cutoff PL model with $E_{\text{cut}} \sim 4$ keV and $\Gamma = 0.2 - 0.3$ (table 3) when the broad 3–20 keV band is incorporated.

These spectral properties of M82 X-1, as well as its luminosity, are very similar to those of NGC 1313 X-1 as recorded with Suzaku, although the values of Γ differ by ~ 0.5 . Based on these similarities, we conclude that M82 X-1 was in the PL state during the present observations. This also implies that M82 X-1 can be regarded as an “ordinary” ULX, rather than a more enigmatic class of accreting source, even though it is rather extreme in terms of the luminosity.

While the cutoff PL is a purely empirical model without physical meaning, it approximates the process of unsaturated thermal Comptonization (section 3.3.3). In fact, the 3–20 keV spectrum of M82 X-1 has also been reproduced reasonably well by the `compTT` model (table 3), invoking a rather low electron temperature of ~ 2.3 keV and a large optical depth of ~ 10 ; the condition is close to a nearly saturated Comptonization. As mentioned in section 3.3.3, the parameters derived here agree very well with those of the same object obtained by Agrawal, Misra (2006) using the 3–10 keV XMM-Newton EPIC data. The Comptonization modeling has also provided reasonable account for the spectra, typically in the 1–10 keV band, of other PL-state ULXs (Kubota et al. 2001a; Fiorito, Titarchuk 2004; Makishima 2007a; Makishima 2007b; Soria et al. 2007; Miyawaki 2008).

A valuable guideline to the understanding of ULXs may be provided by the study of Galactic black-hole binaries (BHBs) (Makishima 2007a). So far, a fair number of BHBs have been observed to leave the canonical standard-disk state, and enter “Very High” state (Miyamoto et al. 1991; McClintock, Remillard 2006), when their luminosities approach the corresponding Eddington limits. Then, the spectrum becomes dominated by a PL-like continuum with $\Gamma \geq 2.4$, plus a soft excess attributable to the underlying disk emission. Such examples include GX339–4 (Miyamoto et al. 1991), GS 1124–68 (Miyamoto et al. 1993), GRO J1655–40 (Kubota et al. 2001a; Kobayashi et al. 2003), XTE J1550–564 (Kubota, Done 2004), GRS 1915+105 (Reig et al. 2003; Done et al. 2004), and 4U 1630–47 (Abe et al. 2005). These Very-High state spectra of BHBs have been interpreted successfully by assuming that a cool standard accretion disk becomes surrounded by a cloud of hot electrons, or a “corona”, so that a significant fraction of the disk photons get Comptonized by the corona (e.g., Done et al. 2007 and references therein). According to Kubota et al. (2001a), the RXTE PCA spectrum of GRO J1655–40 in the Very High state can be understood by invoking a corona with an electron temperature of $T_e \sim 10$ keV and a Compton optical depth $\tau \sim 2$, located above a cool disk which supplies the seed photons. Kobayashi et al. (2003) incorporated the RXTE HEXTE data of the same object and derived $T_e = 75 - 85$ keV and $\tau = 0.45 - 0.65$. Although the solutions thus degenerate, the Compton y -parameter becomes in either case $y \sim 0.3$.

After the initial suggestion by Kubota, Done, & Makishima (2002) and subsequent discussion by several authors (Tsunoda et al. 2006; Mizuno et al. 2007;

Makishima 2007a; Miyawaki 2008), we presume that the PL state of ULXs is analogous to the Very High state of BHBs, and that both appear at near the Eddington luminosity. The bolometric luminosity of M82 X-1 during the present observation is estimated to be $L_{\text{bol}} = (1.5 - 3) \times 10^{40}$ erg s $^{-1}$, by integrating the cutoff PL model. The result does not differ significantly if we instead use the MCD fit. Then, its identification with the Eddington limit leads to a mass estimate as $100 - 200 M_{\odot}$. The mass could be even higher by a few times, if considering that the highest recorded luminosity reaches $\sim 1 \times 10^{41}$ erg s $^{-1}$, and that the Very High state may appear at a luminosity somewhat below the Eddington value (Kubota, Makishima 2004). A possible formation scenario of such an intermediate-mass BH, particularly in close vicinities of galaxy nuclei, has been proposed by Ebisuzaki et al. (2001) and Portegies Zwart et al. (2006). We admit, on the other hand, that the reality of such a cool and thick Compton cloud needs a careful consideration, from the viewpoints of its stability, energetics, and geometry with respect to the seed photon source. These issues are discussed by Agrawal, Misra (2006).

4.3. Another interpretation of the spectrum

Assuming that the PL state of ULXs is analogous to the Very High state of BHBs, we may identify, after some previous works (Mizuno et al. 2001; Watarai et al. 2001; Tsunoda et al. 2006; Makishima 2007a), the CS state of ULXs to the slim-disk state of BHBs that is observed at their highest luminosities (Kubota, Makishima 2004; Abe et al. 2005; Makishima 2007b). This analogy has the following three grounds. First, a ULX generally becomes more luminous, by a factor of 1.5–3 (in the 1–10 keV band), when it makes a transition from the PL state to the CS state (Kubota et al. 2001b; La Parola et al. 2004; Sugiho 2003; Miyawaki 2008). This luminosity relation, including its sense and magnitude, is similar to that observed between the Very High state and the slim-disk state of BHBs. Second, the CS-state spectra of ULXs can be generally reproduced successfully by the variable- p model with $p \sim 0.6$ (e.g., Tsunoda et al. 2006; Mizuno et al. 2007). Finally, when multiple observations of a single CS-state ULX are analyzed by a simple MCD model, we observe the luminosity to scale as $\propto T_{\text{in}}^2$ (Mizuno et al. 2001). The second and third properties agree with the observed behavior of BHBs in their slim-disk state (Kubota, Makishima 2004), as well as predictions by the slim-disk theory (e.g., Watarai et al. 2001; Kawaguchi 2003).

In practice, the above state classification scheme of ULXs can be sometimes rather ambiguous, because a variable- p spectrum with a very high disk temperature takes a rather similar shape to a cutoff PL model. For example, Vierdayanti et al. (2006) applied the variable- p modeling to several PL-state ULXs observed with XMM-Newton. The present M82 X-1 data are subject to the same ambiguity, because the cutoff PL model and the variable- p model have been similarly successful. In fact, Okajima et al. (2006) interpreted an XMM-Newton spectrum of this object (plus some other point sources in-

clusive) as arising from an extreme slim disk with a highly super-Eddington luminosity, formed around a BH of 20–30 M_{\odot} . Even utilizing the broader energy band realized by Suzaku, the degeneracy was not solved, and it remained after removing the source contamination.

Let us briefly examine the slim-disk interpretation of the present Suzaku data for its consistency. The variable- p fit to the XIS plus HXD data gave extremely high disk temperatures as $T_{\text{in}} = 3.0 - 3.5$ keV (table 2 and table 3), regardless of the treatment of the source contamination. It significantly exceeds those observed from other PL-state ULXs, including 1.3–1.9 keV from NGC 1313 X-2 at a 0.4–10 keV luminosity of 0.6×10^{40} erg s $^{-1}$ (Mizuno et al. 2007), and 1.5–1.7 keV from M81 X-9 at a 0.5–10 keV luminosity of 2.4×10^{40} erg s $^{-1}$ (Tsunoda et al. 2006). On the other hand, the temperature index of M82 X-1 was obtained as $p = 0.64 \pm 0.02$ in table 2, or $p = 0.75$ in table 3. Since the latter is consistent with the condition of a standard disk, we may calculate its innermost disk radius R_{in} via $L_{\text{bol}} = 4\pi(R_{\text{in}}/\xi)^2\sigma T_{\text{in}}^4$; here σ is the Stefan-Boltzmann constant, $\xi \sim 1.2$ is a correction factor in Makishima et al. (2000), and the disk inclination is assumed for simplicity as $\sim 60^\circ$.

Taking $T_{\text{in}} = 3.0$ keV (table-3) and $L_{\text{bol}} = (1.5 - 3) \times 10^{40}$ erg s $^{-1}$ (section 4.2), the above procedure yields $R_{\text{in}} = 37 - 52$ km, which corresponds to the last stable orbit of a non-rotating BH with a mass of only 4–6 M_{\odot} . Then, X-1 would be inferred to be shining at 25–35 times the Eddington luminosity. According to a recent numerical study by Vierdayanti et al. (2008), this mass estimate (and hence that of the super-Eddington factor) would not differ by more than a factor of 2, even if the system is in a slim-disk condition. Therefore, we must conclude the source to be in a very deep slim-disk condition. However, this conclusion is not easily reconciled with the measured values of p , which is closer to the standard-disk condition of 0.75 rather than to the limiting slim-disk condition of 0.5. As far as non-rotating BHs are considered, we hence regard the slim-disk interpretation as not being self-consistent; the observed spectrum is simply too hard to be regarded as emission from an optically-thick accretion disk.

If the BH in M82 X-1 is spinning rapidly, its observed properties could be understood more easily in terms of standard accretion disks. This is because the last stable orbit would be then reduced down to $\sim 1/6$ times that of a non-spinning BH of the same mass. This idea was first proposed by Makishima et al. (2000) to explain CS-state spectra of ULXs, and recently applied successfully by Isobe et al. (2008) to a transient ULX. If M82 indeed hosts a maximally rotating BH, the BH mass estimated from the observed R_{in} would increase to 24–36 M_{\odot} . However, we are still left with a super-Eddington factor of 4–9, and have to take into account various relativistic effects (Ebisawa et al. 2003). Therefore, the physical reality of this interpretation is open. In addition, the reported spectral hardening toward lower fluxes (of presumably X-1 itself), based on the RXTE monitoring (Rephaeli, Gruber 2002), is opposite to the behavior of CS-state ULXs (Mizuno et al. 2007). From these consid-

erations, we regard our baseline interpretation presented in section 4.2 as more appropriate.

Incidentally, the state classification scheme of BHBs employed above is based empirically on the observed *luminosity*, but a more physically reasonable scheme should be based on the *accretion rate normalized to the Eddington limit*. Considering that the radiative efficiency itself varies, it is not obvious which of the two states, the Very High state and the slim-disk state, correspond to higher normalized accretion rates. They might even have nearly the same accretion rate, and are controlled by some other parameters including hysteresis effects. In GRO J1655–40 (Kubota, Makishima 2004), in fact, the system was observed to evolve directly from the standard-disk state into the slim-disk state on one occasion when the luminosity was increasing, while from the slim-disk state to the Very High state and then back to the standard-disk state on two occasions during the luminosity descent. A similar hysteresis effect, though less clear, is suggested in the case of 4U 1630–47 (Abe et al. 2005). Clearly, we need deeper understanding of these two high-luminosity states that have been recognized relatively recently.

4.4. Subsidiary Spectral Features

4.4.1. Possible iron edge

Even with the successful three continuum models found in section 3.3.3, we observe some data deficits in the 7–9 keV energy range (figure 8). To account for this structure, we multiplied an absorption edge factor to the continuum models fitted to the XIS and HXD spectra. Regardless of the choice among the three successful continua, the value of χ^2 then decreases by ~ 15 for a decrease of degree of freedom by 2, implying that the edge factor improves the fit with $> 99\%$ significance. The edge energy was constrained as 7.1 ± 0.1 keV, which agrees with the K-edge energy of nearly neutral iron. Its optical depth was obtained as 0.06–0.13, depending on the continuum models and the NXB systematic errors.

The suggested excess Fe-K edge could be reconciled with the adopted low-energy absorption (1.1×10^{22} cm $^{-2}$) if the iron to alpha-element abundance ratio were 5 to 10 times higher than the solar ratio. However, this is opposite to the measured abundance pattern of X-ray emitting materials in M82 (Ranalli et al. 2008), and hence unlikely. An alternative possibility is that X-1 is in fact rather heavily absorbed by a column up to $(4.5 - 9) \times 10^{22}$ cm $^{-2}$ (assuming solar ratios), but the associated strong low-energy absorption is masked by separate softer components.

Yet another possibility is that the spectrum bears a “reflection” component from cold materials, and the Fe-K edge feature imprinted in that component is being observed. To examine this scenario, we removed the Fe-K edge factor from the cutoff PL continuum, and added to it a reflection component, `pextrav` (Magdziarz, Zdziarski 1995), with the reflector iron abundance fixed at 0.6 solar, those of lighter elements at 1.2 solar (Ranalli et al. 2008), and the inclination at 60° . We used the cutoff PL continuum itself as the input to the reflection. Then,

the fit chi-squared decreased (from the original cutoff PL modeling) by ~ 14 , for a decrease of degree of freedom by 1. Therefore, the improvement is comparable to that obtained by applying the Fe-K edge. The reflector solid angle Ω , as seen from the nucleus, is suggested to be relatively large as $\Omega/2\pi \sim 1$, but with a considerable uncertainty, as the associated Compton hump is not well constrained by the HXD data. We consider this scenario most likely to be the case.

4.4.2. Iron emission lines

Let us also discuss the two Fe-K lines detected with the XIS (figure 7). Using Chandra and XMM-Newton, Strickland, Heckman (2007) showed that both these lines are associated primarily to diffuse emission, with insignificant contributions from bright point sources including X-1. Over a circular region of radius $29''$ (0.53 kpc) around the nucleus, they measured the 6.7 keV and 6.4 keV components to have photon fluxes of $(6.9 \pm 4.6) \times 10^{-6}$ ph cm $^{-2}$ s $^{-1}$ and $(4.8 \pm 4.0) \times 10^{-6}$ ph cm $^{-2}$ s $^{-1}$, respectively (from their table 3).

While our data integration radius ($3'$) is significantly larger than that of Strickland, Heckman (2007), diffuse emission in the 2–8 keV band is mostly contained within the $30''$ radius (figure 4f of Strickland, Heckman 2007). Therefore, the Chandra and Suzaku results may be directly compared to the first approximation. From our analysis conducted in section 3.3.1, the stronger 6.7 keV line has a flux of 10.2 ± 2.1 while the weaker 6.4 keV line 4.5 ± 2.0 , both in units of 10^{-6} ph cm $^{-2}$ s $^{-1}$. Thus, the Suzaku and Chandra results agree with each other within respective errors. The observed Fe-K line photons are hence attributed primarily to the diffuse component, but some fraction of the 6.4 keV photons may be associated with the putative reflection component of X-1.

Intriguingly, the co-existing 6.4 keV and 6.7 keV Fe-K lines have also been detected in the diffuse X-ray emission around our Galactic center (Koyama et al. 2007, and references therein) and along the Galactic ridge (Ebisawa et al. 2008). Therefore, we may be observing a similar phenomenon from the M82 central region. However, the emission in our Galactic center is confined within a considerably narrower region of $\lesssim 150$ pc, and its Fe-K photon luminosity, as measured with Suzaku, is 3 orders of magnitude lower than that from the central region of M82 (Tsuru, Nobukawa, and Koyama, a private communication). Presumably, the diffuse emission in M82 is significantly enhanced due to the extreme star-formation activity. Further discussion on the iron emission lines is beyond the scope of the present paper.

4.5. Interpretations Invoking Anisotropic Emission

In addition to the interpretations of ULXs assuming either intermediate-mass BHs (section 4.2) or highly super-Eddington luminosities (section 4.3), a third explanation of these sources invokes strong emission anisotropy enhanced toward us (e.g., King 2002). Among such ideas, we have already argued in section 4.1 against the relativistic beaming scenario. The remaining possibility is geometrical collimation of radiation by a funnel of thick materials

(King 2002). In such cases, we should expect strong spectral signatures due to radiation reprocessing, including Fe-K edge features and fluorescent Fe-K lines, like in some extreme Seyfert 2 galaxies (e.g., Ueda et al. 2007). Indeed, we found the evidence of reflection by nearly neutral materials (section 4.4). However, the observed reprocessor solid angle, $\Omega/2\pi \sim 1$, and the equivalent width of the neutral Fe-K emission line, ~ 20 eV (section 3.3.1), are both far smaller than would be expected ($\Omega/2\pi \gg 1$, and an equivalent width of > 1 keV) when the observed radiation is dominated by the reflected component. Furthermore, no adequate explanation based on the collimation scenario has been presented, either for the two types of ULX spectra, or for the transitions between them. Therefore, the anisotropic radiation interpretation is unlikely to give a successful account of the ULX phenomenon in general.

5. Conclusion

Based on our discussion, we conclude that M82 X-1 was in the PL state during the present Suzaku observation, and was radiating roughly close to, or slightly below, the Eddington luminosity. This leads to a mass estimate of at least $100 - 200 M_{\odot}$, which is in a good agreement with an independent estimate based on the QPO frequency (section 1). We therefore consider M82 X-1 as a genuine intermediate-mass BH, in the sense that it is significantly more massive than those BHs that can be explained by the standard stellar evolutionary scenario.

References

- Abe, Y., Fukazawa, Y., Kubota, A., Kasama, D., & Makishima, K. 2005, PASJ, 57, 629
 Agrawal, V. K., & Misra, R. 2006, ApJ, 638, L83
 Boldt, E. 1987, Phys. Rep., 146, 215
 Cappi, M., et al. 1999, A&A, 350, 777
 Casella, P., Ponti, G., Patruno, A., Belloni, T., Miniutti, G., & Zampieri, L. 2008, MNRAS, tmp.666
 Colbert, E. J. M., & Mushotzky, R. F. 1999, ApJ, 519, 89
 Colbert, E. J. M., & Ptak, A. F. 2002, ApJS, 143, 25
 Dewangan, G. C., Titarchuk, L., & Griffiths, R. E. 2006, ApJ, 637, L21
 Done, C., Gierliński, M., & Kubota, A. 2007, A&A Rev., 15, 1
 Done, C., Wardziński, G., & Gierliński, M. 2004, MNRAS, 349, 393
 Ebisawa, K., Życki, P., Kubota, A., Mizuno, T., & Watarai, K.-Y. 2003, ApJ, 597, 780
 Ebisawa, K., et al. 2001, ApJL, 562, L19
 Ebisuzaki, T., et al. 2008, PASJ, 60, 223
 Fabbiano, G. 1988a, ApJ, 325, 544
 Fabbiano, G. 1988b, ApJ, 330, 672
 Fabbiano, G. 1989, ARA&A, 27, 87
 Feng, H., & Kaaret, P. 2005, ApJ, 633, 1052
 Fiorito, R., & Titarchuk, L. 2004, ApJ, 614, L113
 Freedman, W., et al. 1994, ApJ, 427, 628
 Griffiths, R. E., Ptak, A., Feigelson, E. D., Garmire, G., Townsley, L., Brandt, W. N., Sambruna, R., & Bregman, J. N. 2000, Science, 290, 1325
 Griffiths, R. E., Schwartz, D. A., Schwarz, J., Doxsey, R. E., Johnston, M. D., & Blades, J. C. 1979, ApJ, 230, 21
 Gruber, D. E., Matteson, J. L., Peterson, L. E., & Jung, G. V. 1999, ApJ, 520, 124
 Hirano, A., Kitamoto, S., Yamada, T. T., Mineshige, S., & Fukue, J. 1995, ApJ, 446, 350

- Ishisaki, Y., et al. 1996, PASJ, 48, 237
 Ishisaki, Y., et al. 2007, PASJ, 59, S113
 Isobe, N., Kubota, A., Makishima, K., Gandhi, P., Griffiths, R. E., Dewangan, G. C., Itoh, T., & Mizuno, T. 2008, PASJ, 60, S251
 Kaaret, P., Prestwich, A. H., Zezas, A., Murray, S. S., Kim, D.-W., Kilgard, R. E., Schlegel, E. M., & Ward, M. J. 2001, MNRAS, 321, L29
 Kaaret, P., Simet, M. G., & Lang, C. C. 2006, ApJ, 646, 174
 Kawaguchi, T. 2003, ApJ, 593, 69
 King, A. R., 2002 MNRAS, 336, 445
 Kobayashi, Y., Kubota, A., Nakazawa, K., Takahashi, T., & Makishima, K. 2003, PASJ, 55, 273
 Kokubun, M., et al. 2007, PASJ, 59, S53
 Koyama, K., et al. 2007, PASJ, 59, S245
 Krauss, M. I., Kilgard, R. R., Garcia, M. R., Roberts, T. P., & Prestwich, A. H. 2005, ApJ, 630, 228
 Kubota, A., Done, C., & Makishima, K. 2002, MNRAS, 337, L11
 Kubota, A., & Done, C. 2004, MNRAS, 353, 980
 Kubota, A., Ebisawa, K., Makishima, K., & Nakazawa, K. 2005, ApJ, 631, 1062
 Kubota, A., & Makishima, K. 2004, ApJ, 601, 428
 Kubota, A., Makishima, K., & Ebisawa, K. 2001a, ApJL, 560, L147
 Kubota, A., Mizuno, T., Makishima, K., Fukazawa, Y., Kotoku, J., Ohnishi, T., & Tashiro, M. 2001b, ApJL, 547, L119
 Liu, J., & Bregman, J. 2005, ApJS, 157, 59
 Liu, J., Bregman, J. N., & Irwin, J. 2006, ApJ, 642, 171
 La Parola, V., Fabbiano, G., Elvis, M., Nicastro, F., Kim, D. W., & Peres, G. 2004, ApJ, 601, L831
 Magdziarz, P., & Zdziarski, A. 1995, MNRAS, 273, 837
 Makishima, K. 2007a, Black Holes from Stars to Galaxies – Across the Range of Masses, eds. V. Karas and G. Matt (Proc. f IAU Symp. 238: Cambridge University Press), 209
 Makishima, K. 2007b, Prog. Theor. Phys. Suppl. 169, 214
 Makishima, K., et al. 1989, PASJ, 41, 697
 Makishima, K., et al. 2000, ApJ, 535, 632
 Makishima, K., Maejima, Y., Mitsuda, K., Bradt, H. V., Remillard, R. A., Tuohy, I. R., Hoshi, R., & Nakagawa, M. 1986, ApJ, 308, 635
 Matsumoto, H., & Tsuru, T.G. 1999, PASJ, 51, 321
 Matsumoto, H., Tsuru, T. G., Koyama, K., Awaki, H., Canizares, C. R., Kawai, N., Matsushita, S., & Kawabe, R. 2001, ApJ, 547, L25
 McClintock, J. E., & Remillard, R. A. 2006, Compact stellar X-ray sources, eds. Walter Lewin & Michiel van der Klis (Cambridge Astrophysics Series, No. 39: Cambridge University Press), 157
 Miller J. M., Fabbiano G., Miller M. C., & Fabian A. C. 2003, ApJL, 585, L37
 Mineshige, S., Hirano, A., Kitamoto, S., Yamada, T., & Fukue, J. 1994, ApJ, 426, 308
 Mitsuda, K., et al. 1984, PASJ, 36, 741
 Mitsuda, K., et al. 2007, PASJ, 59, 1
 Miyamoto, S., Iga, S., Kitamoto, S., & Kamado, Y. 1993, ApJL, 403, L39
 Miyamoto, S., Kimura, K., Kitamoto, S., Dotani, T., & Ebisawa, K. 1991, ApJ, 383, 784
 Mizuno, T., Kubota, A., & Makishima, K. 2001, ApJ, 554, 1282
 Mizuno, T., et al. 2007, PASJ, 59, 257
 Miyawaki, R., 2008, PhD Thesis, The University of Tokyo
 Moran, E. C., & Lehnert, M. D. 1997, ApJ, 478, 172
 Mucciarelli, P., Casella, P., Belloni, T., Zampieri, L., & Ranalli, P. 2006, MNRAS, 365, 1123
 Okajima, T., Ebisawa, K., & Kawaguchi, T. 2006, ApJ, 652, L1050
 Pakull, M. W., & Mirioni, L. 2003, Revista Mexicana de Astronomiay Astrofísica Conference Series, 15, 197
 Pellegrini, S., Cappi, M., Bassani, L., Malaguti, G., Palumbo, G. G. C., & Persic, M. 2000, A&A, 353, 447
 Portegies Zwart, S., Baumgardt, H., McMillan, S. L. W., Makino, J., Hut, P., & Ebisuzaki, T. 2006, ApJ, 641, 319
 Ptak, A., Colbert, E., van der Marel, R. P., Roye, E., Heckman, T., & Towne, B. 2006, ApJS, 166, 154
 Ptak, A., & Griffiths, R. 1999, ApJ, 517, L85
 Ranalli, P., Origlia, L., Comastri, A., & Maiolino, R. 2008, MNRAS, 386, 1464
 Reig, P., Belloni, T., & van der Klis, M. 2003, A&A, 412, 229
 Rephaeli, Y., & Gruber, D. 2002, A&A, 389, 752
 Sánchez-Sutil, J. R., Muñoz-Arjonilla, A. J., Martí, J., Garrido, J. L., Pérez-Ramírez, D., & Luque-Escamilla, P. 2006, A&A, 452, 739
 Schaaf, R., Pietsch, W., Biermann, P. L., Kronberg, P. P., & Schmutzler, T. 1989, ApJ, 336, 722
 Soria, R., Baldi, A., Risaliti, G., Fabbiano, G., King, A., La Parola, V., & Zezas, A. 2007, MNRAS, 379, 1313
 Stevens, I. R., Read, A. M., & Bravo-Guerrero, J. 2003, MNRAS, 343, L47
 Stobbart, A.-M., Roberts, T. P., & Wilms, J. 2006, MNRAS, 368, 397
 Strohmayer, T. E., & Mushotzky, R. F. 2003, ApJ, 586, L61
 Strickland, D. K., & Heckman, T. M. 2007, ApJ, 658, S258
 Sugiho, M., 2003, PhD Thesis, The University of Tokyo
 Swartz, D. A., Ghosh, K. K., Tennant, A. F., & Wu, K. 2004, ApJS, 154, 519
 Takahashi, T., et al. 2007, PASJ, 59, S35
 Titarchuk, L. 1994, ApJ, 434, 570
 Tsunoda, N., Kubota, A., Namiki, M., Sugiho, M., Kawabata, K., & Makishima, K. 2006, PASJ, 58, 1081
 Tsuru, T. 1992, Ph.D thesis, The University of Tokyo
 Tsuru, T.G., et al. 2007, PASJ, 59, S269
 Tsuru, T.G., Awaki, H., Koyama, K., & Ptak, A. 1997, PASJ, 49, 619
 Tsuru, T. G., Matsumoto, H., Inui, T., Matsushita, S., Kawabe, R., Harashima, T., Maihara, T., Iwamuro, F. 2004, PTPS, No. 155, 59
 Ueda, Y. et al. 2007, ApJ, 665, 209
 Vierdayanti, K., Mineshige, S., Ebisawa, K., & Kawaguchi, T. 2006, PASJ, 58, 915
 Vierdayanti, K., Watarai, K., & Mineshige, S. 2008, PASJ, 60, 653
 Watarai, K., Mizuno, T., & Mineshige, S. 2001, ApJL, 549, L77
 Watarai, K., Fukue, J., Takeuchi, M., & Mineshige, S. 2000, PASJ, 52, 133
 Watson, M. G., Stanger, V., & Griffiths, R. E. 1984, ApJ, 286, 144

Table 1. Signal and background count rates from HXD-PIN.

	October 4	October 19	October 27	Average
On-source	0.295 ± 0.006	0.325 ± 0.005	0.343 ± 0.006	—
NXB*	0.260	0.280	0.300	—
CXB†	0.018	0.018	0.018	—
Net signal‡	0.016 ± 0.006	0.027 ± 0.005	0.025 ± 0.006	0.023 ± 0.003

* Modeled with *bgd_A*.

† Predicted from the HEAO-1 measurements (Boldt 1987; Gruber et al. 1999).

‡ Net count rate, obtained by subtracting the NXB and CXB from the on-source rate.

Table 2. Best-fit model spectral parameters with 90% confidence errors.*

Models	Parameters	XIS-only†	XIS+PIN‡	NXB+4%§	NXB-4%§
Power-law	Γ	1.67 ± 0.02	1.75 ± 0.02	1.77 ± 0.02	1.73 ± 0.02
	$\chi^2/\text{d.o.f}$	318.6/174	606.8/182	809.1/182	464.9/182
Brems	T (keV)	$14.8^{+0.8}_{-0.7}$	$13.6^{+0.6}_{-1.0}$	$13.6^{+0.8}_{-0.4}$	$13.5^{+0.8}_{-0.5}$
	$\chi^2/\text{d.o.f}$	223.9/174	292.2/182	408.3/182	242.0/182
Cutoffpl	Γ	$0.76^{+0.13}_{-0.15}$	$0.77^{+0.08}_{-0.15}$	$0.55^{+0.08}_{-0.17}$	$0.89^{+0.13}_{-0.10}$
	E_{cut} (keV)	$5.8^{+1.0}_{-0.8}$	$5.7^{+0.5}_{-0.7}$	$4.7^{+0.4}_{-0.6}$	$6.8^{+1.5}_{-0.8}$
	$\chi^2/\text{d.o.f}$	183.7/173	193.6/181	228.6/181	202.1/181
CompTT	T_e (keV)	2.5 ± 0.1	2.5 ± 0.1	2.4 ± 0.1	2.8 ± 0.1
	τ	8.3 ± 0.4	8.0 ± 0.4	8.6 ± 0.4	7.4 ± 0.4
	$\chi^2/\text{d.o.f}$	184.5/173	197.2/181	203.5/181	239.4/181
Diskbb	T_{in} (keV)	2.77 ± 0.04	2.79 ± 0.04	2.75 ± 0.04	2.80 ± 0.04
	$\chi^2/\text{d.o.f}$	224.8/174	243.4/182	239.8/182	312.8/182
Variable- p	T_{in} (keV)	$3.38^{+0.32}_{-0.20}$	$3.58^{+0.28}_{-0.18}$	$3.47^{+0.22}_{-0.07}$	$3.53^{+0.50}_{-0.21}$
	p	0.64 ± 0.02	0.63 ± 0.02	0.63 ± 0.02	0.63 ± 0.02
	$\chi^2/\text{d.o.f}$	183.4/173	191.9/181	225.1/181	220.0/181

* The absorbing column density is fixed at $1.1 \times 10^{22} \text{ cm}^{-2}$.

† Using the XIS FI and BI spectra in the 3.2–10 keV band.

‡ From the XIS and HXD-PIN joint fit.

§ When the modeled NXB spectra are systematically over- or under-estimated by 4%.

Table 3. Same as table 2, but considering contamination from surrounding sources

Models	Parameters	Case 1*	Case 2†
Power-law	Γ	1.64 ± 0.03	1.71 ± 0.04
	$\chi^2/\text{d.o.f}$	538.0/182	303.9/182
Brems	T (keV)	18.2 ± 1.1	$13.5^{+2.4}_{-0.9}$
	$\chi^2/\text{d.o.f}$	384.4/182	239.0/182
Cutoffpl	Γ	$0.27^{+0.02}_{-0.04}$	$0.17^{+0.06}_{-0.04}$
	E_{cut} (keV)	4.2 ± 0.1	3.7 ± 0.1
	$\chi^2/\text{d.o.f}$	193.2/181	193.1/181
CompTT	T_e (keV)	2.30 ± 0.03	$2.33^{+0.04}_{-0.08}$
	τ	9.7 ± 0.2	$9.2^{+0.2}_{-0.3}$
	$\chi^2/\text{d.o.f}$	196.8/181	199.9/181
Diskbb	T_{in} (keV)	3.09 ± 0.07	$2.95^{+0.07}_{-0.10}$
	$\chi^2/\text{d.o.f}$	192.7/182	195.0/182
Variable- p	T_{in} (keV)	3.09 ± 0.07	$2.95^{+0.07}_{-0.11}$
	p	$0.75^{+0.01}_{-0.02}$	$0.75^{+0.02}_{-0.03}$
	$\chi^2/\text{d.o.f}$	192.7/181	194.9/181
Flux ‡	(2–10 keV)	1.2	0.7

* The case when spectra of the fainter contaminant sources (except X-2) were removed.

† The case when spectra of both the fainter sources and X-2 were removed.

‡ In units of 10^{-11} erg s $^{-1}$ cm $^{-2}$. Depends no more than 10% on the spectral models.

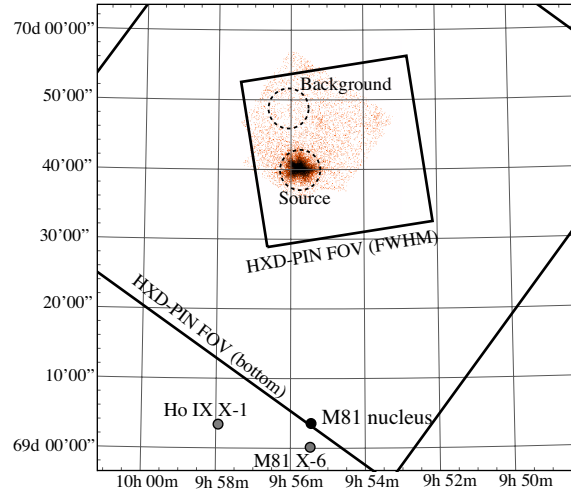


Fig. 1. A background-inclusive 2–10 keV XIS 0 image from the second observation. The smaller and larger squares show the FWHM and full-width at zero transmission FOVs of HXD-PIN, respectively. Dashed circles show the source and background regions used for the XIS analysis. A filled small circle indicates the location of the M81 nucleus, whereas two gray circles those of the two ULXs in this field, M81 X-6 and Holmberg IX X-1 (Fabbiano 1988a).

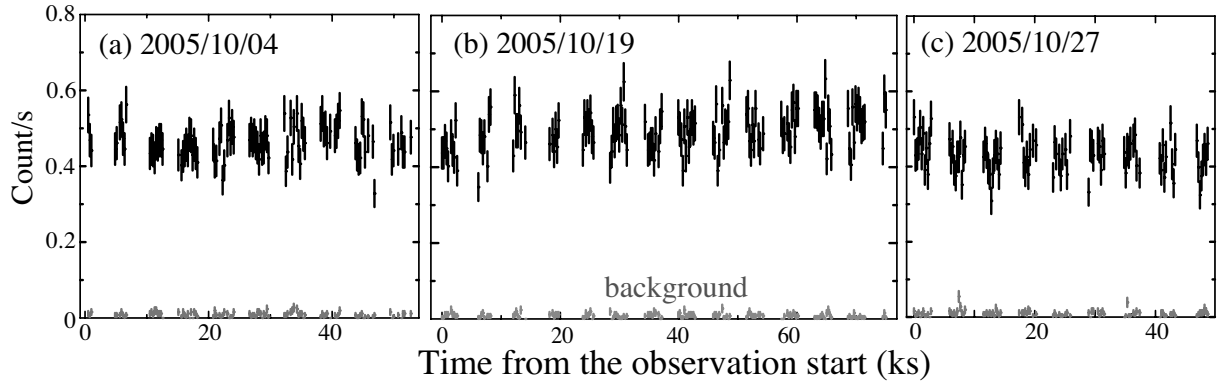


Fig. 2. XIS 0 light curves in the 2–10 keV band extracted from the source (black) and background (gray) regions, acquired on (a) October 4, (b) October 19, and (c) October 27. The bin width is 256 s.

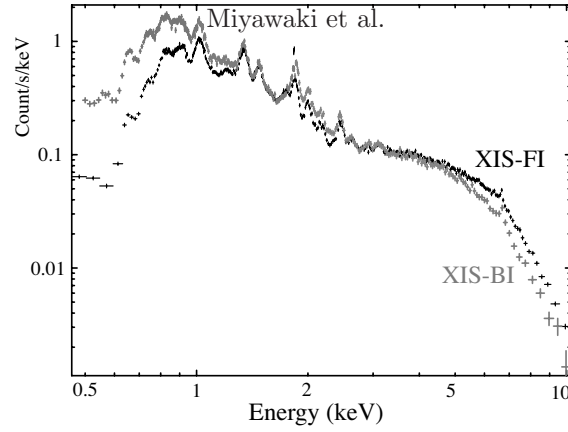


Fig. 3. Background-subtracted XIS spectra of the core region of M82, averaged over the three observations. The instrumental response is included. The FI (three cameras summed) and BI CCD data are shown in black and gray, respectively.

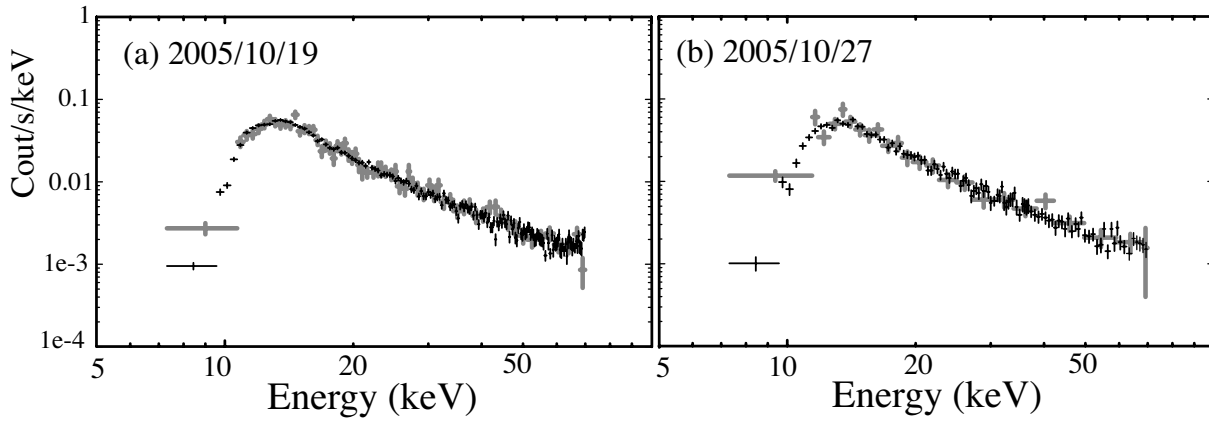


Fig. 4. Earth-occultation spectra of HXD-PIN (black) obtained on (a) October 19 and (b) October 27, compared with the modeled non X-ray background (gray) to be observed during the same time periods.

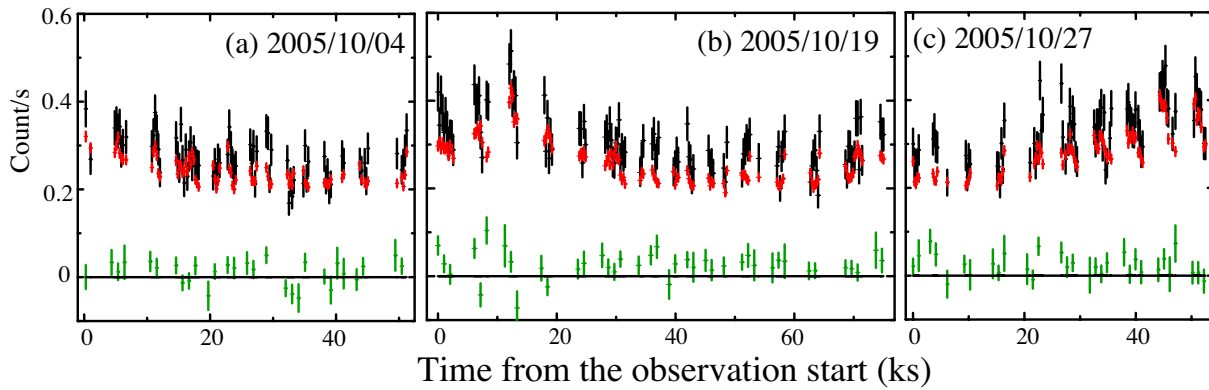


Fig. 5. The 12–20 keV light curves of the M82 region acquired with HXD-PIN on (a) October 4, (b) October 19, and (c) October 27. The observed raw data are shown in black, while the modeled NXB data in red, both using a binning of 256 s. Green data points show the signals remaining after subtracting the NXB and the expected CXB, binned into 1024 s.

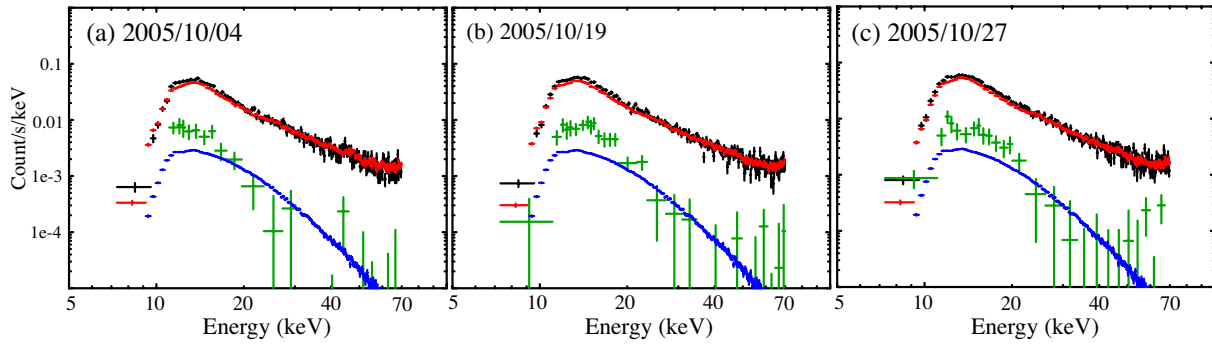


Fig. 6. Time-averaged HXD-PIN spectra obtained on (a) October 4, (b) October 19, and (c) October 27. Each panel shows the observed spectrum (black), the modeled NXB spectrum (red), the signals remaining after subtracting the NXB (green), and the expected CXB spectrum (blue).

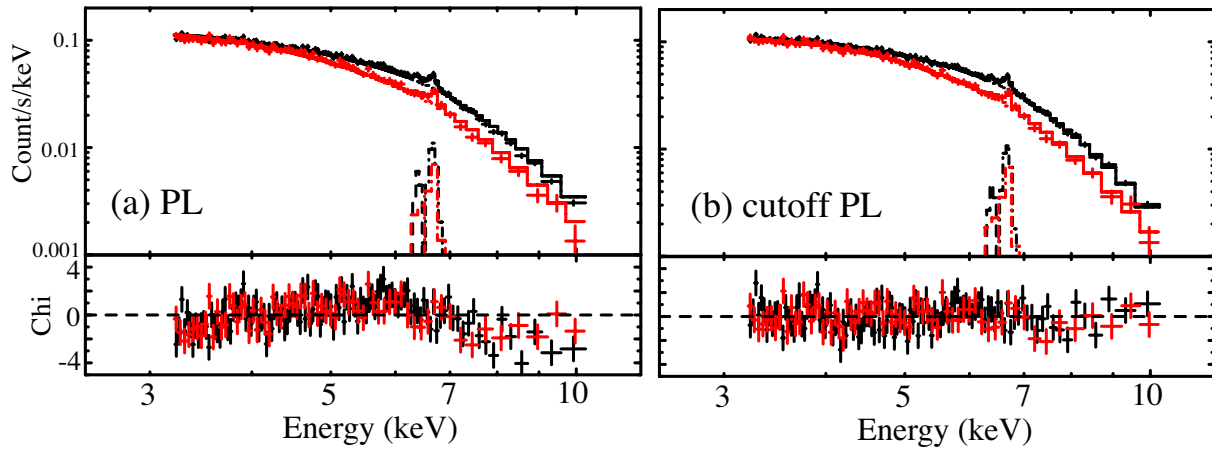


Fig. 7. (a) A 3.2–10 keV portion of the XIS FI (black) and BI (red) spectra in figure 3, presented together with the best-fit absorbed power-law plus gaussian model (upper panel) and the fit residuals (lower panel). (b) The same as panel a, but the power-law is replaced by a cutoff power-law.

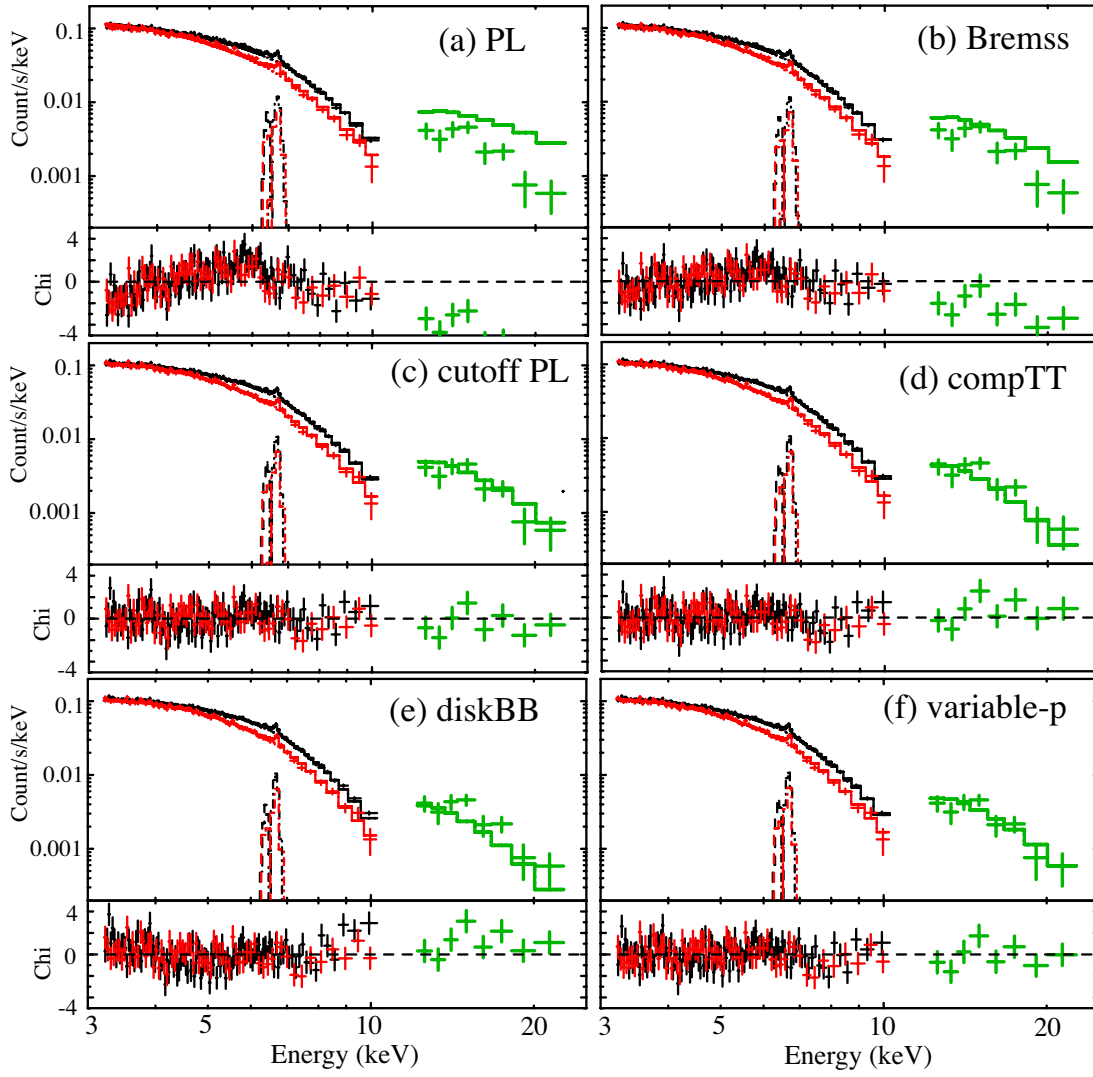


Fig. 8. The same as figure 7, but the fit jointly incorporates the HXD-PIN spectrum (green) from which the NXB (nominal) and CXB are both subtracted. The employed fitting models are; (a) power-law, (b) bremsstrahlung, (c) cutoff power-law, (d) *compTT*, (e) *diskbb*, and (f) *variable-p* disk model.

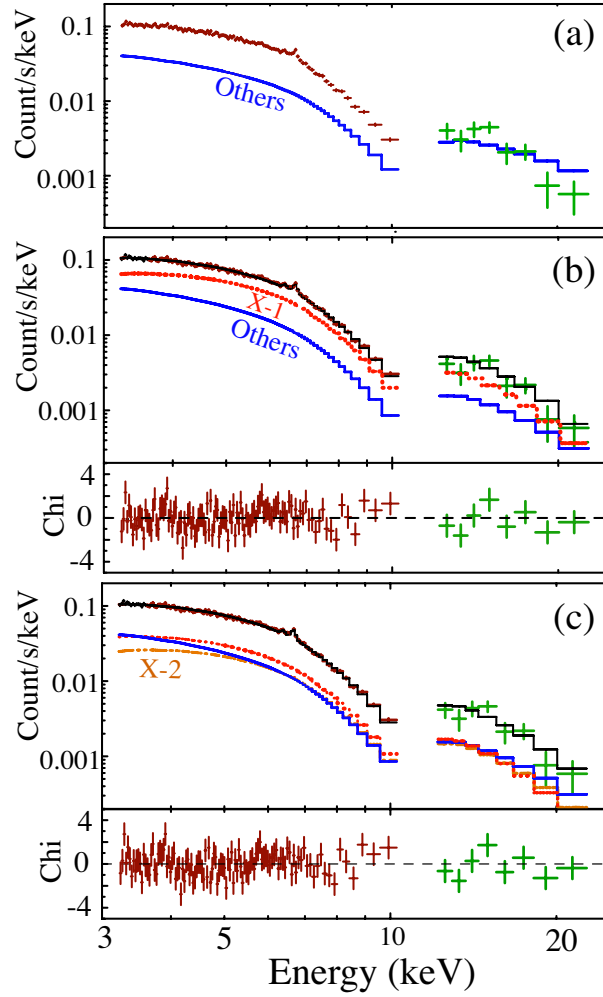


Fig. 9. The same joint XIS plus HXD fits as figure 8, but incorporating estimated contributions from the contaminating sources (table 3). The data points from XIS-FI and HXD-PIN are shown in brown and green, respectively, while the XIS-BI data are omitted for clarity. The two Gaussians, though included, are omitted for the same reason. (a) The case when the summed spectrum of “the other fainter sources”, estimated in the XIS band (blue), extends into the HXD-PIN range with a PL shape. (b) The case (Case 1) when the spectrum of the fainter sources (blue) is approximated by a 10 keV brems model, with its normalization fixed in the XIS range. The X-1 spectrum (red) is modeled by a cutoff PL with a free shape and free normalization. The total model prediction is indicated in black, and the fit residuals are shown in the lower panel. (c) The same as panel b, but when the X-2 contribution is included as a fixed model (orange) represented by another cutoff PL model (Case 2; see text). In the HXD-PIN range, the three constituent components nearly overlap.